CEAS Aeronautical Journal
https://doi.org/10.1007/s13272-024-00792-0

ORIGINAL PAPER

Flight testing of laser-optical techniques for future optical air data sensors

Oliver Kliebisch[1] · Raoul-Amadeus Lorbeer[1] · Peter Mahnke[1] · Matthias Damm[1] · Georg Dietz[2] · Thomas Fuchs[2] · Sebastian Burwitz[2]

Received: 28 March 2024 / Revised: 25 October 2024 / Accepted: 4 November 2024

Abstract

Optical air data sensors, which can serve as alternatives or supplements to traditional air data systems, have been a subject of ongoing research. These remote sensing optical sensors offer the advantage of measuring primary air data parameters in undisturbed airflow. As active sensors, they can self-diagnose, associating each measurement with an uncertainty and accounting for signal loss due to factors such as icing or light blocking, thus avoiding silent false measurements. In this paper, we discuss a recent flight test campaign of optical measurement techniques for potential development into air data sensors for future aircraft. We used laser Doppler anemometry, which relies on aerosol scattering of laser light, to observe the Doppler shift of scattered light from multiple directions. This enables the reconstruction of the full wind vector and the retrieval of true air speed, angle of attack, and angle of sideslip. A second instrument used tunable diode laser absorption spectroscopy, which measures an individual transition of molecular oxygen in the A band, in order to extract the static pressure from the observed collisional broadening. The techniques were implemented as airborne research instruments on the DLR's Dassault Falcon 20 aircraft and tested in two campaigns in 2022 under different atmospheric conditions and dynamic maneuvers. We present results from these campaigns, focusing on general sensor performance, measurement rates, accuracy, and experimental challenges that need to be addressed for future applications.

Keywords Optical air data · Sensors · Avionics · Lasers · Lidar · Spectroscopy · LDA · TDLAS

✉ Oliver Kliebisch
oliver.kliebisch@dlr.de

Raoul-Amadeus Lorbeer
raoul.lorbeer@dlr.de

Peter Mahnke
peter.mahnke@dlr.de

Matthias Damm
matthias.damm@dlr.de

Georg Dietz
georg.dietz@dlr.de

Thomas Fuchs
thomas.fuchs@dlr.de

Sebastian Burwitz
sebastian.burwitz@dlr.de

[1] Institute of Technical Physics, German Aerospace Center, Pfaffenwaldring 38-40, Stuttgart 70569, Baden-Württemberg, Germany

[2] Flight Experiments, German Aerospace Center, Münchener Str. 20, Weßling 82334, Bavaria, Germany

List of symbols

1U	Rack height unit
α	Scaling factor
$\boldsymbol{\Delta f}_{\mathrm{D}}$	Line-of-sight Doppler shifts
$\boldsymbol{K}$	LDA unit vectors (beam direction)
$\boldsymbol{v}_{\mathrm{long}}$	Longitudinal velocity vector (m/s)
$\boldsymbol{v}_{\mathrm{r}}$	Reconstructed velocity vector (m/s)
$\boldsymbol{v}_{\mathrm{trans}}$	Transversal velocity vector (m/s)
$\boldsymbol{W}$	LDA weights matrix
γ_{L}	Lorentzian broadening, half width at half maximum ($\mathrm{cm}^{-}1$)
$\gamma_{\mathrm{O_2,air}}$	Foreign-broadening coefficient
$\gamma_{\mathrm{O_2,self}}$	Self-broadening coefficient
λ	Laser wavelength (m)
σ_{G}	Gaussian broadening, standard deviation ($\mathrm{cm}^{-}1$)
A	Area of the normalized absorption line
CH_4	Methane
CO_2	Carbon dioxide
f_{D}	Doppler shift frequency (Hz)
f_{LO}	Local oscillator frequency (Hz)

Published online: 26 November 2024

f_L	Laser frequency (Hz)
H_2O	Water molecule
I	Optical power (W)
I_0	Initial optical power (W)
I_{ref}	Reference optical power (W)
k_B	Boltzmann constant
L	Optical path length (cm)
N	Number density (molecule/cm^3)
n	Temperature coefficient
N_2	Molecular nitrogen
p	Pressure (Pa)
p_0	One standard atmosphere in Pa (Pa)
$S(T)$	Temperature-dependent absorption line strength (cm^{-}1/(molecule cm^{-}2))
T	Temperature (K)
T_0	Reference temperature = 296 K
$V(x, \sigma_G, \gamma_L)$	Voigt function
ADC	Analog-to-digital converter
AoA	Angle of attack
AoS	Angle of sideslip
Ar	Argon
DAC	Digital-to-analog converter
DFB-laser	Distributed-feedback laser
DLR	Deutsches Zentrum für Luft- und Raumfahrt (German Aerospace Center)
FL	Flight level
FPGA	Field programmable gate array
HITRAN	High-resolution transmission
ISA	International standard atmosphere
LDA	Laser doppler anemometer
LO	Local oscillator
LOS	Line of sight
SSD	Solid state drive
TAS	True air speed
TAT	Total air temperature
TDLAS	Tuneable diode laser absorption spectroscopy
TRA	Temporary restricted area

1 Introduction

Air data sensors are a crucial component of an aircraft's avionics system, providing vital information about the current flight configuration. The conventional Pitot-static system, complemented by temperature probes and alpha/beta vanes, has long been the central sensor system for delivering primary data on impact pressure, static pressure, static temperature, angle of attack, and angle of sideslip [12]. By applying the assumptions of the International Standard Atmosphere equations [1], derived quantities, such as indicated air speed, barometric altitude, and vertical speed, can be calculated.

However, a persistent problem with the electro-mechanical probes of the Pitot-static system is the risk of false readings or total malfunction under icing conditions, even with heating [6]. Additionally, due to their proximity to or placement within the fuselage, calibrating these sensors is a labor-intensive process, and it is essential that no flight conditions outside the calibrated envelope are encountered.

Shortly after the invention of the laser, the first laser-optical velocimetry methods were conceived and flight-tested in the early 1970 s [17, 19]. This innovation prompted the concept of a fuselage-flush optical air data system [7, 9], and numerous instruments have been developed and flight-tested over the ensuing decades [2, 3, 11, 16, 18]. Optical air data sensors offer the advantage of being "self-diagnosing," meaning that signal loss or degradation is detectable and does not result in unnoticed erroneous measurements. Additionally, the measurement point can be situated outside the aircraft's boundary layer, requiring only a fuselage-flush optical aperture.

Progress in this field has been slow due to the lack of compact, robust laser sources and contemporary real-time digital signal processing hardware. With the emergence of reliable, robust, and miniaturizable laser-optical systems (e.g., fiber lasers and photonic integration) and more sophisticated signal processing, it has become increasingly feasible to develop and flight-test optical air data sensors.

In this paper, we present the results of our recent flight campaign, which aimed to test research instruments for the optical measurement of true airspeed, angle of attack, angle of sideslip, static pressure, and static temperature. We will detail the flight campaign, test conditions, and two of the instruments used in this study: a fiber-coupled vector laser Doppler anemometer (LDA) and a fiber-coupled tunable diode laser absorption spectroscopy (TDLAS) system. Key aspects were to perform a proof-of-concept experiment, to identify potential implementation issues and to assess the feasibility of both techniques as optical air data sensors in one combined flight experiment.

2 Research instruments

2.1 Laser doppler anemometer

2.1.1 Flow velocimetry with LDA

Laser Doppler anemometry (LDA) is a well-established technique for measuring flow velocities in wind tunnels. A specific implementation, known as reference-beam laser LDA, is illustrated in Fig. 1. In this setup, a continuous wave laser with frequency f_L is sentthrough a circulator and focused onto the measurement volume. Light scattered from particles, which can range in size from about

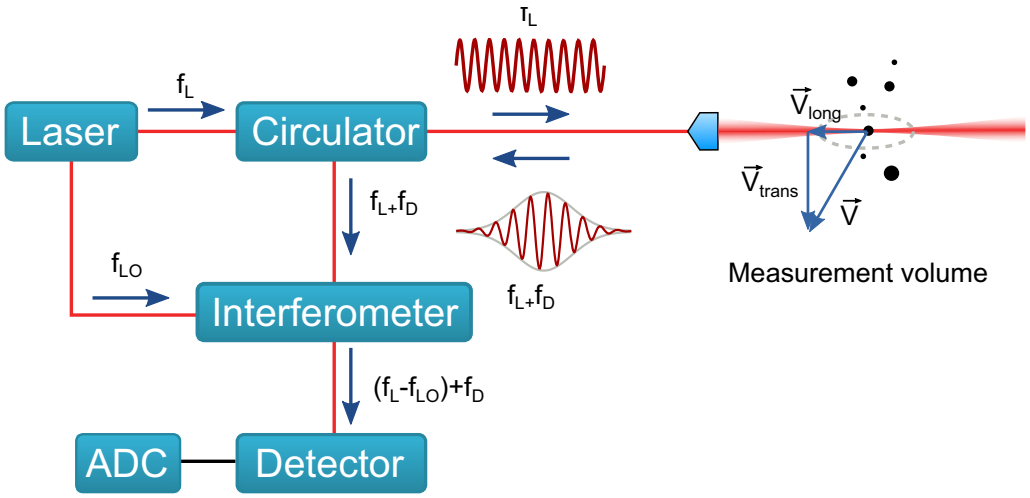

Fig. 1 Functional principle of a single channel reference-beam laser Doppler anemometer

$1/10$ of the wavelength in diameter to macroscopic sizes, is collected by the same optics and directed back into the instrument, where it is separated from the incoming beam by the circulator. Each burst of scattered light, with its Doppler-shifted frequency $f_L + f_D$ (where f_D is the Doppler shift), is made to interfere with a reference beam of light tapped from the original laser source at frequency f_{LO}. This results in an interferometric beat signal that isolates the beat frequency $(f_L - f_{LO} + f_D)$. In cases where $f_L = f_{LO}$, homodyne detection is performed, measuring only the absolute value of the Doppler shift. Otherwise, heterodyne detection is used, which also conveys the sign of the Doppler shift.

Each LDA channel measures the line-of-sight velocity, given by $v_{LOS} = -\lambda/2 f_D$, where λ is the laser wavelength.

2.1.2 LDA instrument for the flight campaigns

We have implemented four LDA channels in the form of a three-height-unit 19-inch rack module combined with a separate two-height-unit FPGA-based processing unit [13, 14]. The full system architecture is depicted in Fig. 2. The system is split into three main components: first, the LDA rack module which contains a laser system, interferometers, detectors as well as power management. The whole system is powered from the 28V bus. Second, the transceiver optics which send and receive the laser light into the outside of the aircraft and receive the scattered light. Third, a data acquisition and processing unit based on the MicroTCA.4.1 standard. The LDA rack module is shown in Fig. 3. The LDA system is built in a master oscillator power amplifier architecture (MOPA),

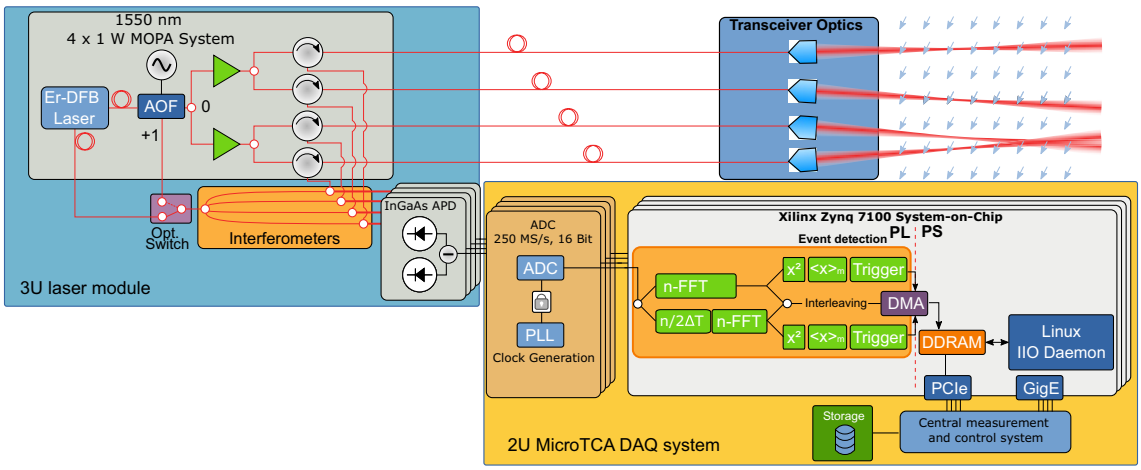

Fig. 2 System architecture of the four-channel laser Doppler anemometer. The system consists of the LDA rack module housing all electro-optical components and all fiber optics, the transceivers and the MicroTCA module housing all the data acquisition and processing equipment

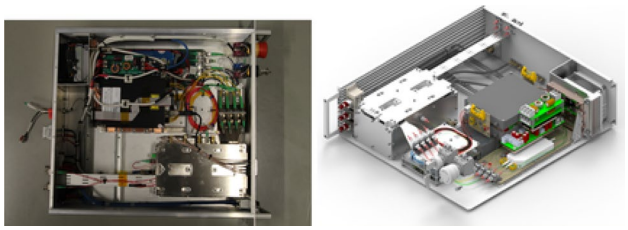

Fig. 3 Left: Photograph of the top view into the LDA rack box showing the interior setup of the system. Right: CAD-Rendering of the LDA rack module with side and top covers removed, showing how the laser system is stacked and heat is transferred to a forced air cooling department in the back of the module

where the light of a narrow linewidth 1550nm fiber laser is amplified and split into four channels of 1W output power each. Despite this amount of laser power, the use of 1550nm allows the reach of a short nominal ocular hazard distance and operate the instrument safely. The interferometric signal of each channel is detected by a pair of Indium–Gallium–Arsenide avalanche photodetector diodes, digitized and transferred to the FPGA processing system.

The FPGA pre-processors detect the individual bursts on each channel and record raw data streams on the command of the instrument operators [14]. The bursts from each channel are fitted with a Gaussian, resulting in the estimated Doppler shift and its uncertainty. As each channel measures independent particle bursts at random time instances, all data points are regularized onto a regular time grid by a constant spline interpolation. The reconstruction of the relative wind vector $\hat{\boldsymbol{v}}_r$ is a linear regression problem of the following form [13]:

$$\hat{\boldsymbol{v}}_r = -\frac{\lambda}{2}\left(\boldsymbol{K}^T\boldsymbol{W}\boldsymbol{K}\right)^{-1}\boldsymbol{K}^T\boldsymbol{W}\Delta\boldsymbol{f}_{\mathrm{D}} \tag{1}$$

Here $\boldsymbol{K}$ is a matrix containing the unit vectors of the beam direction for each LDA channel, $\boldsymbol{W}$ is a diagonal weights matrix containing the uncertainties of each Doppler shift, and $\Delta\boldsymbol{f}_{\mathrm{D}}$ are the Doppler shifts of all LDA channels written as components of a vector. By performing the uncertainty analysis, each reconstructed vector can be associated with uncertainties for each component and therefore in contrast to a Pitot-probe, the LDA instrument permanently outputs its measurement uncertainty.

The laser light from each channel is directed through a transfer fiber to a singlet aspheric lens, which projects the fiber end into the air surrounding the aircraft at a distance of either 500mm or 1000 mm, depending on the configuration chosen for the specific measurement flight. The boundary between the cabin and the exterior of the aircraft is an interface plate, as shown in Fig. 4. Each channel is imaged through its own 15mm thick anti-reflection coated fused silica window. All windows are angled at 15 circ relative to the

Fig. 4 The optical aperture plate showing four 4" anti-reflection coated windows. Each channel is imaged through this window and the beam path will cross about 500 mm away from the fuselage in a common point

nadir direction. A strictly perpendicular orientation would result in a zero Doppler shift. The directions must differ for each channel to enable successful vector reconstruction.

2.2 Tuneable diode laser absorption spectroscopy

2.2.1 Pressure detection with TDLAS

The TDLAS system was designed to detect static pressure outside of the fuselage. To deduce a pressure from a gaseous medium with a spectroscopic technique, it is necessary to resolve the shape of at least one absorption line of a species present in the medium. Absorption lines in gaseous media are extremely narrow and only span several GHz. Therefore, a highly resolving spectroscopy technique is necessary. TDLAS is able to achieve few MHz resolution at several 100 THz of electromagnetic frequency and therefore it is perfectly suited to resolve the shape of a single absorption line. Furthermore, additional factors have to be taken into account to form a useful avionic sensor. These allow to deduce the species which shall be analyzed with TDLAS. The chosen species for spectroscopy should be distributed almost homogeneously in the atmosphere so a measurement under all flight conditions will be possible. Therefore, water vapor (H_2O), even though being shown to be applicable to avionic pressure detection [5], is unsuitable for a broad application as a spectroscopic pressure sensor in avionics, due to its concentration spanning orders of magnitude in the atmosphere. Furthermore, the chosen species should have spectroscopically addressable absorption lines. This eliminates molecular nitrogen (N_2) and argon (Ar) from the list of candidates which leaves molecular oxygen (O_2), carbon dioxide (CO_2) and methane (CH_4). The last aspect lies in the wavelength of the addressable absorption lines as well as the mixing of those. Since the system is meant to be integrated in an

airplane, we chose an all fiber-optic-based approach and therefore technologies with wavelengths below 1650 nm. This makes molecular oxygen the most interesting candidate since the oxygen A-band around 760 nm does not interfere with other molecular absorption lines present in the atmosphere. As already mentioned, the TDLAS technique has been shown to be able to deduce static pressure in a flight experiment [5]. To deduce the pressure from the line shape, it is advantageous to understand the macroscopic properties of the air which lead to the final line shape. The quantum-mechanical transitions in the oxygen A-band in themselves are extremely narrow and would not be resolvable with realistic TDLAS systems. Due to the temperature of the gas, the molecules have a Gaussian velocity distribution along a given axis which leads to a Gaussian-shaped Doppler broadening of the absorption line. The second effect is based on collisions between the molecules which interrupt an absorption process by changing the molecule's momentum. Collisions lead to a Cauchy–Lorentz distribution in the spectrum. Since both effects happen simultaneously, the final line profile is a Voigt profile which represents the convolution of both line shapes [10].

$$V(x,\sigma_G,\gamma_L)=\int_{-\infty}^{\infty}\frac{e^{-u^2/(2\sigma_G^2)}}{\sigma_G\sqrt{2\pi}}\cdot\frac{\gamma_L}{\pi((x-u)^2+\gamma_L^2)}du \tag{2}$$

The absorption line is measured by measuring the optical power loss due to transmission through a known path of gaseous media:

$$I(\lambda)=I_0(\lambda)\cdot e^{-S(T)\cdot V(\lambda-\lambda_0)\cdot N\cdot L} \tag{3}$$

with the reference optical power I_0, absorption line strength S(T), the number density N, temperature T and the length of the beam path L.

By measuring a reference optical power I_{ref} from the laser, the initial optical power $I_0=\alpha I_{ref}$ can be measure for a given scaling factor α. Rearranging Eq. (3) yields:

$$\ln\left(\frac{I(\lambda)}{I_{ref}(\lambda)}\right)=-S(T)\cdot N\cdot L\cdot V(\lambda-\lambda_0)+\ln(\alpha) \tag{4}$$

$$\ln\left(\frac{I_{ref}(\lambda)}{I(\lambda)}\right)=A\cdot V(\lambda-\lambda_0)+\ln(\alpha) \tag{5}$$

Additionally, measuring the static air temperature allows for the calculation of the Gaussian broadening σ_G and introduces the known value into the fitting procedure. Ideally, only absorption strength as the area of the normalized absorption line A and the collision broadening as the width of the Cauchy–Lorentz distribution γ_L will have to be fitted. In reality, at least the offset $\ln(\alpha)$ has to be determined as well. More sophisticated background models may be found in the literature [5]. While the absorption strength correlates with the density of the oxygen, the collision broadening only depends on the rate at which collisions occur. This again depends on the effective collisional cross sections of the oxygen molecules, with themselves $\gamma_{O_2,self}$ and all other species $\gamma_{O_2,air}$ as well as the number density N of the gas and the speed of the molecules.

The number density is included in the line area A. Using literature values (HITRAN database [8]) for the absorption line strength S and the Boltzmann constant k_B as well as the known optical path length L, the ambient pressure may be deduced by [5]:

$$p=\frac{\gamma_L\cdot p_0\left(\frac{T_0}{T}\right)^n-\left(\gamma_{O_2,self}+\gamma_{O_2,air}\right)\frac{k_B\,T}{S\,L}\cdot A}{\gamma_{O_2,air}} \tag{6}$$

2.2.2 Technical implementation of the TDLAS system

After thorough testing in a laboratory environment [15], the TDLAS system was implemented as an all optical fiber-based system for the flight experiments. All electronics, power supply, fiber optic components as well as the laser systems were accommodated in a 3U 19-inch rack box. Figure 5 shows the basic set of components. The dashed line indicates all components within the custom rack box system. The setup is connected to a rack-mounted PC including a digital–analog conversion (DAC) and analog-to-digital conversion (ADC) card (National Instruments, PCIe-6374). The DAC creates a linear voltage sweep which is converted to a linear current sweep by the laser driver (Koheron, CTL200-1), which will be converted to an almost linear frequency sweep by the DFB laser (Eagleyard, EYP-DFB-0760-00003-1500-BFY12-0002). The laser light then is split into reference and measurement radiation. The measurement radiation is sent via a polarization maintaining fiber to the optical transceiver extensions on top of the airplane (compare Fig.6). The reference half of the laser light is then split againsuch that99% are routed to a simple reference optical power measurement with a photodiode. To calibrate the frequency axis of the TDLAS technique, the remaining 1% is routed through an all fiber-based Mach–Zehnder interferometer with an optical path difference of 3m (2m delay fiber). The generated beat signal is then recorded with a third photodiode and encodes the spectral axis. All photodiodes are digitized with the ADC. The implementation of the system is shown in Fig.5b. The system is supplied with 28 V main power, which is connected to the fuses to distribute power to the internal components, the PTC heaters, the PC as well as the transceiver photodiodes. Internal components are the main PCB, which generates the supply voltage of

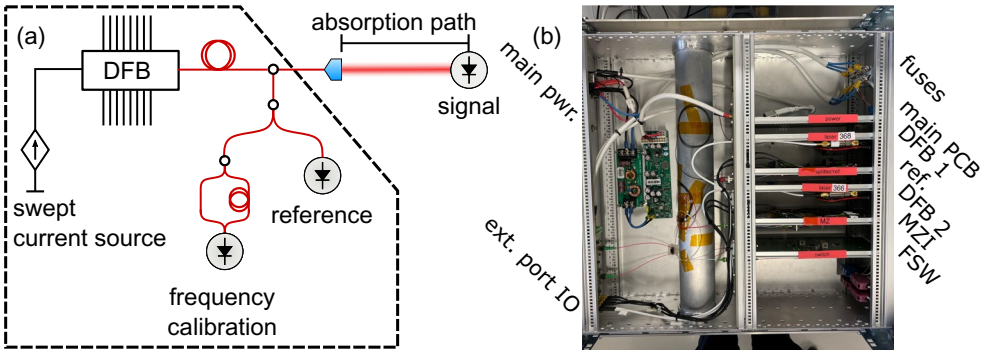

Fig. 5 **a** Schematic setup of the TDLAS system. The tunable, Distributed FeedBack (DFB) laser diode is driven by a tunable current source. The periodically sweeping laser frequency is sent to the absorption path capturing the absorption signal with a photodiode. Furthermore, referencing photodiodes capture the reference laser power as well as the sweep rate using a Mach–Zehnder interferometer. **b** Photograph of the rack box implementation of the TDLAS system. The system is supplied with 28 V main power, which is connected to the fuses to distribute power to the internal components, the PTC heaters, the PC as well as the transceiver photodiodes. Internal components are main PCB, the first DFB (DFB 1), the second DFB (DFB2), the reference photodiode (ref.), the MZI (MZI) as well as a fiber switch (FSW) electrical and optical IO (ext. port IO) which connects to the transceivers as well as the ADC of the PC

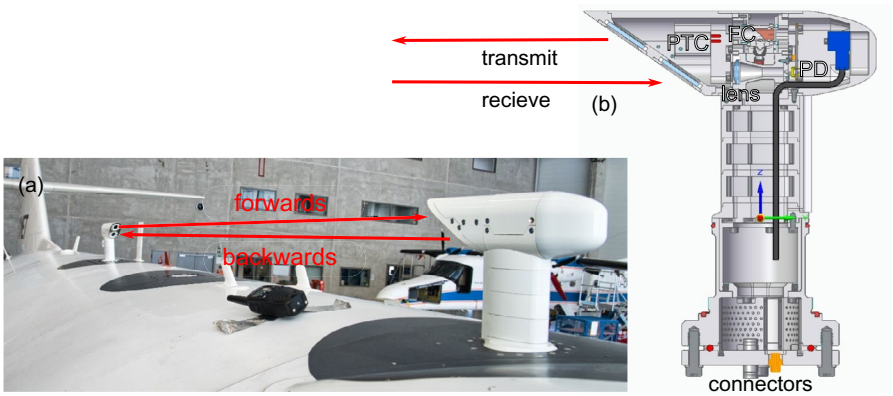

Fig. 6 **a** Photograph of the installed optical transceiver extensions. **b** CAD cross section through the optical transceiver. Indicated are the PTC heater (PTC), the fiber collimator (FC), the photodiode (PD), the collection lens (lens) as well as the optical and electrical feedthrough. (all) Beam paths and directions are indicated by the red arrows

the photodiode amplifiers as well as establishes the serial connection to the laser drivers and the fiber switch (FSW). Both DFB lasers (DFB 1 and DFB 2) are integrated on a custom PCB, carrying the laser driver and connecting to power as well as signal distribution. Photodiode for reference and MZI are integrated directly on additional PCBs, which also support the fiber optical components for power-splitting and the MZI. The fiber switch allows choosing the emission direction of the transceiver elements. Electrical and optical IO (ext. port IO) connections are supported at the back of the rack box to connect to the transceivers as well as the ADC of the PC.

At any given time, only one laser system is active and the beam is only send into one direction. This results in four relevant states for the optical system. The first DFB laser (LD366) at $13,146.5737\text{cm}^{-1}$ is switched on and sends the laser beam backward (LD366 b) or forwards (LD366 f) or the second DFB laser (LD368) at $13,146.5767\text{cm}^{-1}$ is switched on and sends the laser beam backwards (LD368 b) or forwards (LD368 f). Even though an ideal TDLAS system would be installed flush with the fuselage, due to the restrictions given by the research aircraft, the installation of two exterior extensions was chosen. The exterior optical transceivers have integrated amplified photodiodes to create a differential signal as close as possible to the photodiode itself, as well as customized reflective fiber collimators to send the polarized laser light through color glass windows at the Brewster angel. Because of this, no anti-reflective coating is needed and solar background is reduced significantly. The direction of the beams is indicated in Fig.6a. Thereby, the system can be evaluated at two heights relative to the fuselage. To reduce complexity, beam steering was omitted and the system relies on the stiffness of the airplane itself. During the flight experiments, it became apparent that the fuselage deformed more than anticipated, which led to an optomechanical limitation of the beam path for flight levels (FL) higher than FL 240. In those conditions, the laser beam did deviate from its ground level path by more than 7 mm and could not reach the detector anymore. The internal structure of the optical transceivers is indicated in Fig. 6b. The

connectors on the inside of the fuselage support electrical and fiber-optical feed-through. The fiber is collimated with a reflective fiber collimator (FC) to transmit the measurement light along the top of the aircraft. Transmitter and receiver are switched in position at the opposing transceiver such that the receiving beam enters the lens at the bottom path and is focused onto the photodiode (PD). Furthermore, a PTC heater is installed to heat the transmitting and receiving windows which are angled at the Brewster angle to omit reflective losses.

Finally, ADC data as well as logging data from the internal systems was stored on SSDs in flight and evaluated for pressure in an offline workflow. During the flight experiments, the spectrograms were shown in real time.

3 Mission profiles of the flight campaigns

The Dassault Falcon 20-E5 research aircraft, operated by the DLR Flight Experiments and depicted in Fig. 7, was utilized as the carrier and test aircraft for the research instruments. Modifications were made to the lower fuselage of the aircraft, which already had two viewports with apertures of approximately 500mm in diameter. A new aperture plate was installed, featuring four optical windows for the laser Doppler anemometry instrument, each tilted at 15° relative to the nadir direction. The second viewport was fitted with a pre-existing segmented lidar window. Atop the fuselage, two antenna ports, typically used for trace gas inlets, were equipped with two newly developed transmitter/receiver attachments. These attachments extended about 20cm from the fuselage and functioned as a closed-path optical measurement path for the spectroscopy pressure sensor.

The aircraft is outfitted with a noseboom featuring a five-hole probe, as well as other sensors that deliver a high quality calibrated reference data set. This set includes standard air data parameters and additional environmental data, such as humidity, temperature, and wind speeds, as well as attitude and accelerometer data.

Two campaigns totaling 44 flight hours were conducted, as shown in Fig. 8. The primary parameters which were under investigation due to their influence on the measurement performance or them being the primary measurement quantity are shown in Tab. 1. The first campaign, comprising approximately 20 flight hours, consisted of six flights conducted between April 4th and April 27th, 2022. The

Fig. 7 Photo of the Dassault Falcon 20-E5 research aircraft of the DLR flight experiments. The plane is equipped with a noseboom. The opened shutter door (the black section in the bottom of the fuselage) shows the two circular viewports holding the optical interfaces for the laser Doppler anemometry instrument and a lidar window used for a filtered Rayleigh scattering instrument

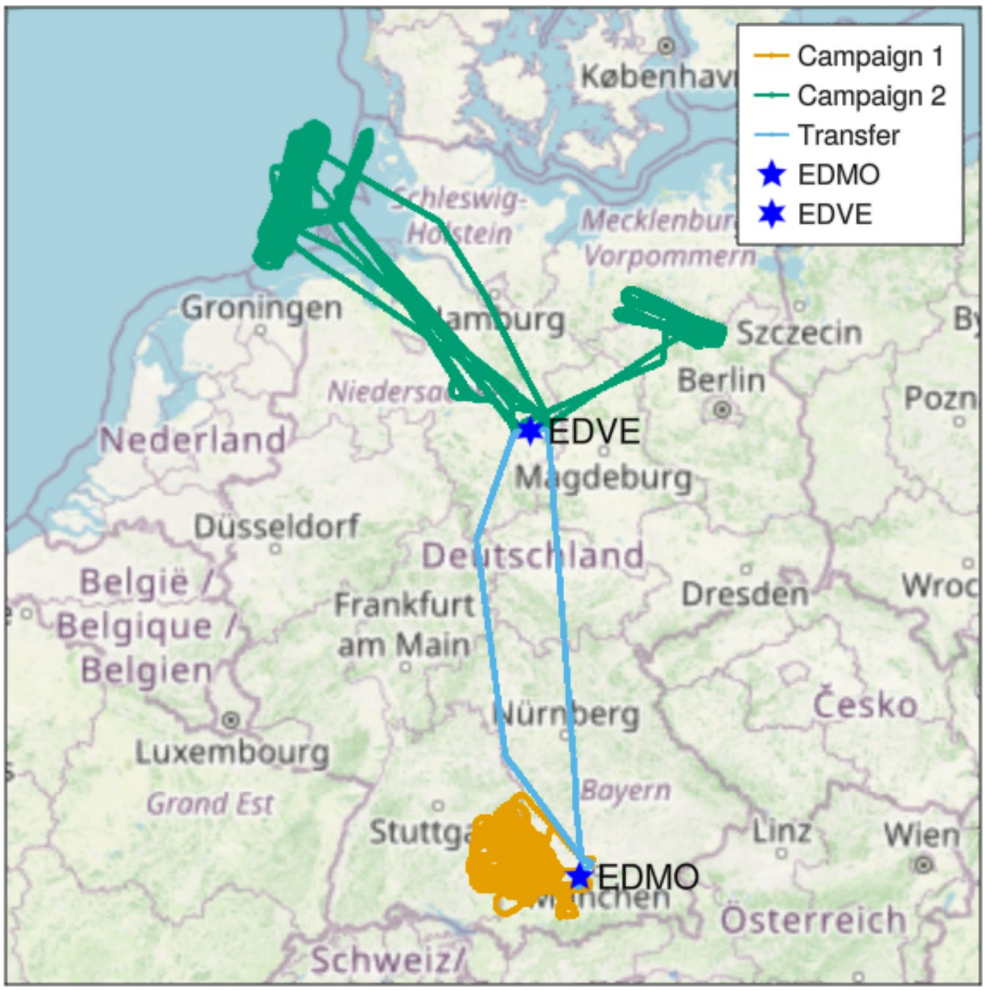

Fig. 8 Map of the flight routes of the two campaigns as well as the transfer flights which have been used for measurements as well. The airports of Oberpfaffenhofen (ICAO: EDMO) and Braunschweig–Wolfsburg (ICAO: EDVE) served as basis for the campaigns

Table 1 Campaign profiles and how different parameters have been varied and evaluated

Parameter under evaluation	Flight situation
Angle of attack	Different flight speeds at constant height
Angle of side slip	Steady-heading sideslip and during curve flight
True air speed	Variation of speed
Flight patterns	• Racetracks
	• Full circles at half-bank, full-bank, 45° and 60°
	• Phugoid oscillations at 15° and 15° pitch angle
Signal rate	Flight environment (aerosol concentration)
	•Flight at different altitude
	•Flight over lidar reference station
	•Flight within planetary boundary layer
	•Marine aerosol
	•Urban aerosol
	•Saharan dust

Oberpfaffenhofen airport served as the base for this campaign, with all flights taking place within the temporary reserved airspace in the Allgäu area (TRA Allgäu). This campaign primarily aimed to assess basic functionality. Thus, it included tests of racetrack patterns at various altitudes up to flight level 400, as well as variations in angle of attack and angle of sideslip. In each flight, a low pass was made over the ground lidar (ceilometer) station at Hohenpeissenberg to allow the comparison of the instrument's performance with a reference measurement of aerosol content in the air masses.

The second campaign, based in Braunschweig, lasted approximately 24 flight hours and included transfer flights between October 17th and October 28th, 2022. The aircraft was equipped with the instrumentation in Oberpfaffenhofen, enabling the transfer flights to serve as measurement flights as well. All except one flight took place over the North Sea, where clear air conditions were encountered and more dynamic patterns, such as phugoid oscillations, full circles at high bank angles, and other maneuvers, were tested. The LDA instrument, in particular, benefited from a high variability in atmospheric conditions, with clear air conditions serving as a challenging test case due to the technique's reliance on the presence of atmospheric aerosols.

4 Results

4.1 Laser Doppler anemometry

Figure 9 presents a comprehensive evaluation of data from one of the flights in the first campaign. The data measured by the LDA is compared to the noseboom reference, depicted as a solid red line for all parameters. In addition to true airspeed (TAS), angle of attack (AoA) and angle of sideslip (AoS), the GPS altitude, measurement rate (combining all four channels), and residual histograms are displayed. The R^2 correlation values for TAS, AoA and AoS are 0.955, 0.982 and 0.370. The reduced correlation for the angle of sideslip is mainly caused by just performing a coarse alignment of the LDA viewport adapter when mounting it into the fuselage of the aircraft. Generally, there is good correlation between the LDA and the noseboom data. Due to the interpolation algorithm, increased noise is currently observed in the LDA measurements. This noise can be reduced by employing filtering at the expense of measurement bandwidth or using a more sophisticated approach, such as a cascaded Kalman filter, to regularize and fuse the individual channels into a vector output. It should be noted that only a rough calibration has been performed to account for mounting errors of the LDA optics, as well as a linear aerodynamic correction function. This correction accounts for the mounting position, at which location a rectification of the flow field

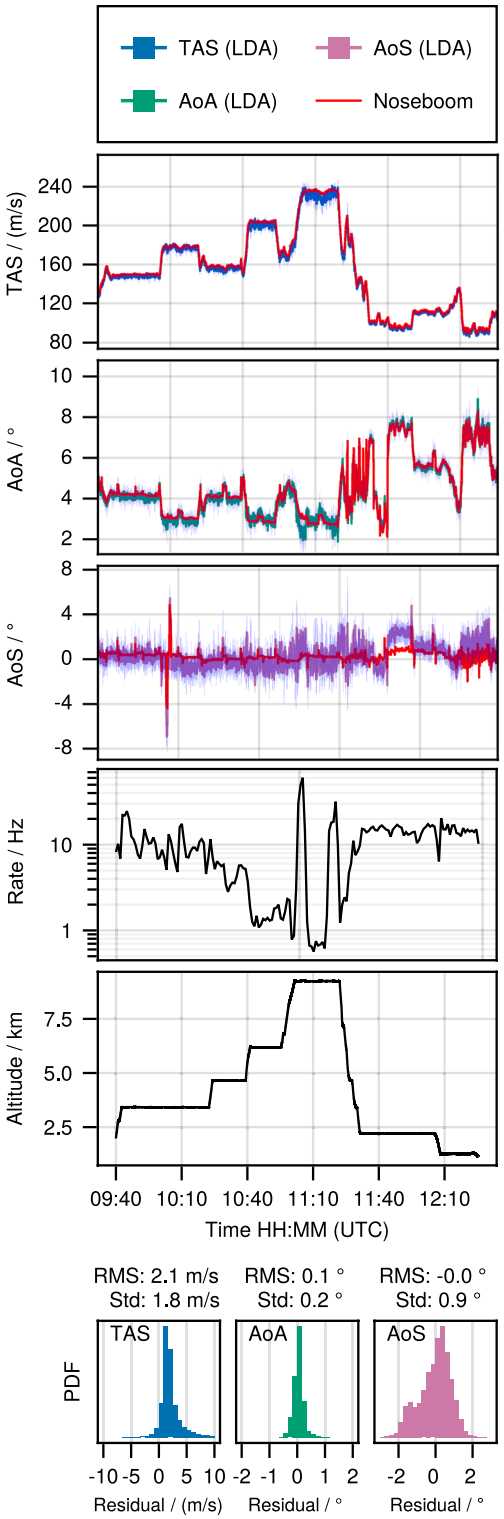

Fig. 9 Results of the LDA instrument for April 11th, 2022

is anticipated. For future integration, a mounting position less prone to such errors should be chosen.

The measurement rate is variable and falls below 1 Hz at high altitudes or low aerosol content. Throughout the

campaigns, we observed varying performance in terms of measurement rate, which is only slightly dependent on altitude above the planetary boundary layer, but more influenced by general weather conditions. This suggests that some aerosol background was consistently present [4]. We identified several unoptimized factors, such as photodetection and digital processing, which negatively impacted the measurement rate. We believe that with an improved system, the measurement rate can be increased by at least one order of magnitude.

4.2 Tuneable diode laser spectroscopy

The first offline evaluation of the TDLAS data after the flight experiments showed a significant deviation from the reference static pressure of the nose boom data. Figure 10 displays the evaluated pressure from the TDLAS signal against the documented timestamp. Both DFB lasers evaluating two different line transitions in the oxygen A-band show consistent results. In this flight, the forward direction (f) was essentially used for measurements. In comparison, the pressure evaluated from the TDLAS shows a significant offset and the system drops at 12:17 UTC+2 (compare Fig. 10) compared to the static pressure from the on-board reference system. This is strongly correlated to the TAS at the same time, such that it is obvious that the system still is influenced by the aerodynamics close to the fuselage. Since TAT is correlated to TAS, an eminent change is also visible there with the change in the evaluated TDLAS pressure. Therefore, both metrics could be suitable for the correction of the TDLAS pressure.

Both TAS and TAT were tested to be included in a linear correction of the spectroscopically evaluated pressure p_{TDLAS}. Eventually, TAT did show the better results. The resulting effective TDLAS pressure p_{eff} is significantly closer to the reference sensor and does not show the speed-dependent pressure change any longer.

$$p_{\mathrm{eff}} = p_{\mathrm{TDLAS}} + (TAT - \Delta T) \cdot a \tag{7}$$

Nevertheless, the corrected p_{eff} still showed a nonlinear correlation to the reference static pressure which was addressed with a second correction using a polynomial of second order.

$$p_{\mathrm{TDLAS,\,corr}} = p_{\mathrm{eff}} \cdot b + p_{\mathrm{eff}}^2 \cdot c + \Delta p \tag{8}$$

The resulting corrected evaluation is shown in Fig. 11 and was achieved with the values given in Table 2. It was possible to introduce this correction for the whole flight spanning 2 and $\frac{1}{2}$ hours. Unfortunately, this

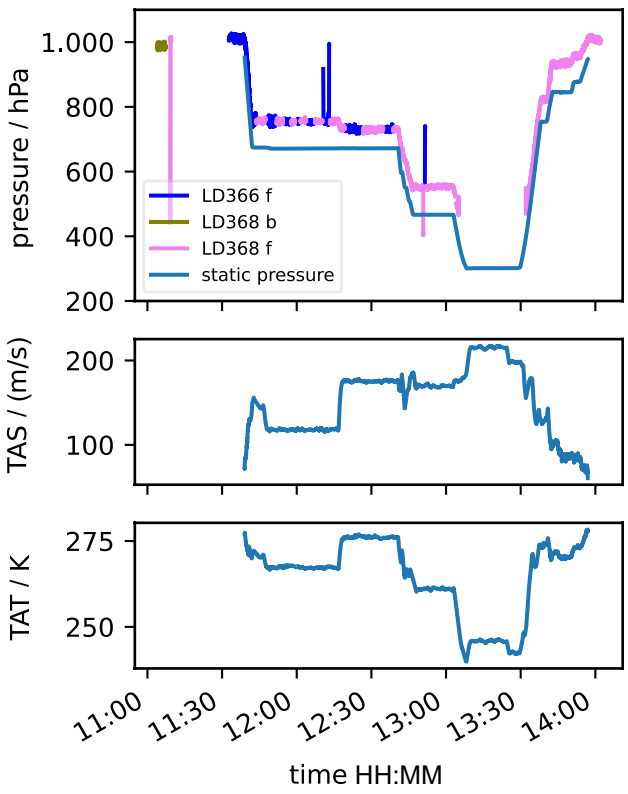

Fig. 10 Plot of uncorrected first flight data from April 4th, 2022. Potted are static pressure, spectroscopic pressure, static air temperature (SAT) and true air speed (TAS) against UTC+2 time

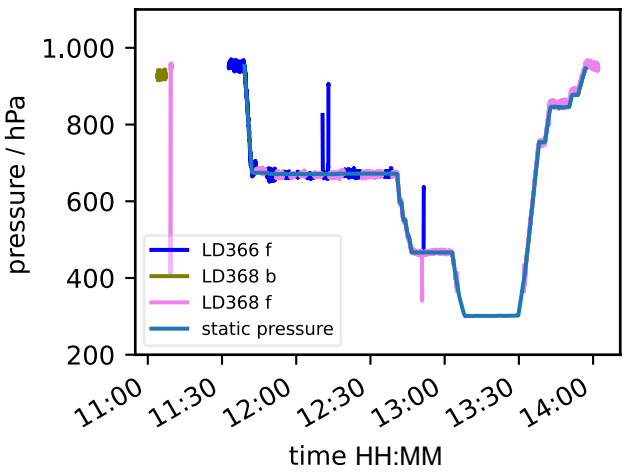

Fig. 11 Plot of corrected first flight data from April 4th, 2022. Potted are static pressure and spectroscopic pressure against UTC+2 time. Correction parameters are given in Table 2

Table 2 Parameters for non-linear correction of TDLAS pressure

a	b	c	ΔT	Δp
$3.11\frac{\mathrm{hPa}}{a}$	$0.681\frac{1}{\mathrm{hPa}}$	$1.7 \times 10^{-4}\frac{1}{\mathrm{hPa}^2}$	260K	36hPa

phenomenological correction is not suitable for all flight days. A more general correction will be part of future investigations.

5 Discussion and conclusion

5.1 LDA

In this paper, we have presented the flight test results for a four-channel fiber-coupled reference beam laser Doppler anemometer (LDA). The system was tested in-flight for over 40 h and remained operational throughout. Our findings demonstrate a strong correlation between the LDA values and a noseboom reference sensor. The remaining inaccuracies in the results can be mitigated through a more systematic calibration of mounting errors of the LDA sensor transceiver and the implementation of correction functions that account for the aerodynamic influences at the measurement location. The measurement rates varied between 1Hz and over 100Hz depending on atmospheric conditions. Notably, even in clear air conditions, a measurable signal was observed, albeit at a lower measurement rate of around (or less than) 1Hz.

Several strategies can be pursued to enhance the measurement rate in clear air conditions. First, optimizing real-time signal processing presents an immediate opportunity for improvement. Second, the current use of APD-based photodetectors limits the sensor's SNR, and substituting them with alternative photodetectors could yield a fivefold increase in SNR. Third, the system was constructed using fiber connectors rather than spliced, polarization-optimized splices. Further options, such as increasing the laser power, could be explored, but these may have negative consequences for the size, weight, and power requirements of an LDA-based optical air data sensor.

5.2 TDLAS

We were able to demonstrate a strong correlation between a TAT corrected spectroscopically deduced pressure and the reference system for static pressure over the course of an experimental flight. Aperture limitations of the optical path combined with the specific aerodynamic-dependent mechanical properties of the fuselage of the airplane limited TDLAS measurements to FL 240 and below. Since TAT is not only dependent on the flight level and the TAS, but also on the weather conditions and other external influences it is not surprising that the correction based on the TAT does only apply for our first flight. More surprisingly, the full correction of the spectroscopically deduced pressure did perform better using a linear TAT correction than a linear TAS correction. Therefore, a thorough evaluation on which flight data parameters are best suited for the overall evaluation of the TDLAS data still has to be performed.

5.3 General conclusion

The flight campaign demonstrated the fundamental feasibility of the tested instruments for measuring the respective air data parameters. Accuracy, signal-to-noise ratio, and measurement rates need to be addressed in future work to meet the requirements for air data instruments. Given the current state of knowledge, and considering that encountered limitations were partially attributed to the specific implementation in this flight campaign, improvements leading to improved measurement rates and accuracy seem possible with enhanced instruments and a dedicated calibration against the aircraft's noseboom. Both techniques offer the potential for further miniaturization through deeper optoelectronic integration, elimination of interfaces between separate electronic devices, and more streamlined real-time digital signal processing.

Acknowledgements We thank Samantha Siegert for proof-reading this manuscript.

Funding Open Access funding enabled and organized by Projekt DEAL.

Data availability Data sets generated during the current study are available from the corresponding author on reasonable request.

Declarations

Conflict of interest The authors declare no Conflict of interest.

References

1. Standard Atmosphere. – ISO 2533:(1975)
2. Bogue, R., McGann, R., Wagener, T., Abbiss, J., Smart, A.: Comparative optical measurements of airspeed and aerosols on a DC-8 aircraft. In: ICIASF'95 Record. International Congress on Instrumentation in Aerospace Simulation Facilities IEEE, S. 56–1 (1995)
3. Bogue, R.K.: Recent Flight-test Results of Optical Airdata Techniques. Version: 1993. https://books.google.de/books?id=

jYE4AQAAIAAJ. National Aeronautics and Space Administration, Office of Management, Scientific and Technical Information Program, (AIAA-92/4086). – Forschungsbericht (1993)
4. Brock, C.A., Williamson, C., Kupc, A., Froyd, K.D., Erdesz, F., Wagner, N., Richardson, M., Schwarz, J.P., Gao, R.-S., Katich, J.M., Campuzano-Jost, P., Nault, B.A., Schroder, J.C., Jimenez, J.L., Weinzierl, B., Dollner, M., Bui, T., Murphy, D.M.: Aerosol size distributions during the Atmospheric Tomography Mission (ATom): methods, uncertainties, and data products. Atmos. Meas. Tech. **12**, 3081–3099 (2019). https://doi.org/10.5194/amt-12-3081-2019
5. Buchholz, B., Afchine, A., Ebert, V.: Rapid, optical measurement of the atmospheric pressure on a fast research aircraft using open-path TDLAS. In: Atmospheric Measurement Techniques **7**(11), 3653–3666 (2014). https://doi.org/10.5194/amt-7-3653-2014
6. Cao, Y., Tan, W., Wu, Z.: Aircraft icing: An ongoing threat to aviation safety. Aerosp. Sci. Technol. **75**, 353–385 (2018). https://doi.org/10.1016/j.ast.2017.12.028
7. DC, Defense Science Board W.: Report of the Defense Science Board Task Force on the National Aerospace Plane (NASP).– Forschungsbericht (1988)
8. ...Gordon, I.E., Rothman, L.S., Hargreaves, R.J., Hashemi, R., Karlovets, E.V., Skinner, F.M., Conway, E.K., Hill, C., Kochanov, R.V., Tan, Y., Wcisło, P., Finenko, A.A., Nelson, K., Bernath, P.F., Birk, M., Boudon, V., Campargue, A., Chance, K.V., Coustenis, A., Drouin, B.J., Flaud, J.-M., Gamache, R.R., Hodges, J.T., Jacquemart, D., Mlawer, E.J., Nikitin, A.V., Perevalov, V.I., Rotger, M., Tennyson, J., Toon, G.C., Tran, H., Tyuterev, V.G., Adkins, E.M., Baker, A., Barbe, A., Canè, E., Császár, A.G., Dudaryonok, A., Egorov, O., Fleisher, A.J., Fleurbaey, H., Foltynowicz, A., Furtenbacher, T., Harrison, J.J., Hartmann, J.-M., Horneman, V.-M., Huang, X., Karman, T., Karns, J., Kassi, S., Kleiner, I., Kofman, V., Kwabia-Tchana, F., Lavrentieva, N.N., Lee, T.J., Long, D.A., Lukashevskaya, A.A., Lyulin, O.M., Makhnev, VYu., Matt, W., Massie, S.T., Melosso, M., Mikhailenko, S.N., Mondelain, D., Müller, H.S.P., Naumenko, O.V., Perrin, A., Polyansky, O.L., Raddaoui, E., Raston, P.L., Reed, Z.D., Rey, M., Richard, C., Tóbiás, R., Sadiek, I., Schwenke, D.W., Starikova, E., Sung, K., Tamassia, F., Tashkun, S.A., Vander Auwera, J., Vasilenko, I.A., Vigasin, A.A., Villanueva, G.L., Vispoel, B., Wagner, G., Yachmenev, A., Yurchenko, S.N.: The HITRAN2020 molecular spectroscopic database. In: Journal of Quantitative Spectroscopy and Radiative Transfer **277**, 107949 (2022). https://doi.org/10.1016/j.jqsrt.2021.107949. ISSN 0022-4073
9. Handbook, Prototype: Optical Air Data System (OADS). In: Reports, Proposals, UTOS 1989 (1987)
10. Hanson, Ronald K., Spearrin, R.M.: Goldenstein, Christopher S.: Spectroscopy and optical diagnostics for gases. Cham : Springer. – xxv, 279 pages : illustrations, diagrams S (2016). https://doi.org/10.1007/978-3-319-23252-2. – ISBN 9783319232515
11. Jentink, H.-W., Kannemans, H., Verbeek, M.-J.: In-flight evaluation of an optical standby air data system. National Aerospace Laboratory NLR – Forschungsbericht (2010)
12. Jäckel, R., Gutiérrez-Urueta, G., Tapia, F.: A review on Pitot tube icing in aeronautics: Research- design and characterization - future trends. In: Flow Measurement and Instrumentation 81, 102033 (2021). https://doi.org/10.1016/j.flowmeasinst.2021.102033. – ISSN 0955–5986
13. Kliebisch, O., Damm, M., Mahnke, P.: Airborne four channel fiber coupled vector laser Doppler anemometer system. In: Appl. Opt. 62, Sep, Nr. 25, 6746–6753 (2023). https://doi.org/10.1364/AO.498171
14. Kliebisch, O., Mahnke, P.: Real-time laser Doppler anemometry for optical air data applications in low aerosol environments. In: Review of Scientific Instruments 91, 09, Nr. 9, 095106 (2020). https://doi.org/10.1063/5.0014389. – ISSN 0034–6748
15. Lorbeer, R.-A., Bittner, M., Kliebisch, O., Mahnke, P.: Pressure Detection With Mach-Zehnder Linearized Tunable Diode-Laser Absorption Spectroscopy. In: IEEE Open Journal of Instrumentation and Measurement 3, 7000210, 1-10 (2024). https://doi.org/10.1109/OJIM.2024.3396843
16. Mandle, J.: A laser anemometer reference for AIR data calibration. In: Proceedings of the IEEE 1988 National Aerospace and Electronics Conference IEEE, S. 300–308 (1988)
17. Muñoz, R.-M., Mocker, H.-W., Koehler, L.: Airborne Laser Doppler Velocimeter. In: Appl. Opt. 13, Dec, Nr. 12, 2890–2898 (1974). https://doi.org/10.1364/AO.13.002890
18. Watkins, C.-B., Richey, C.-J., Tchoryk Jr, P., Ritter, G.-A., Hays, P.-B., Nardell, C.-A., Willis, T.-C., Urzi, R.: Molecular optical air data system (MOADS) flight experiment. In: Laser Radar Technology and Applications VIII Bd. 5086 SPIE, S. 236–245 (2003)
19. Yeh, Y.: Cummins, H. Z.: Localized fluid flow measurements with an He-Ne laser spectrometer. In: Applied Physics Letters 4, 12, Nr. 10, 176-178. https://doi.org/10.1063/1.1753925. – ISSN 0003–6951 (1964)